Thermal-hydraulic test and analysis of the ENEA TF conductor sample for the EU DEMO fusion reactor

Thermal–hydraulic test and analysis of the ENEA TF conductor sample for the EU DEMO fusion reactor

R. Bonifetto, P. Bruzzone, V. Corato, L. Muzzi, *Senior Member, IEEE*, L. Savoldi, *Member, IEEE*, B. Stepanov, R. Zanino, *Senior Member, IEEE*, A. Zappatore

***Abstract*—The ENEA conductor for the EU DEMO Nb_3Sn Toroidal Field (TF) magnets, cooled by supercritical He, features a rectangular cross section with two small pressure relief channels ("holes"), separated from the cable bundle by means of a flat spiral, twisted together with the last cabling stage. A well instrumented short sample of the ENEA TF conductor has been tested in SULTAN at SPC, Villigen (Switzerland) in 2016, aimed at its thermal-hydraulic characterization, and the test results are presented here. A correlation for the friction factor in the small holes is derived, best fitting the results of a set of computational fluid dynamics (CFD) simulations. The new correlation (combined with existing correlations for the He friction factor in the bundle region) is shown to allow a proper reproduction of the measured hydraulic characteristic of the conductor. The heat slug propagation tests are used to calibrate the hole-to-bundle heat transfer coefficient in the 4C thermal-hydraulic code and to estimate the characteristic length for the homogenization of the He temperature on the conductor cross section, following a localized thermal perturbation.**

***Index Terms*—CFD, CICC thermal-hydraulic characterization, DEMO, superconductor sample test.**

I. Introduction

THE superconducting (SC) magnet system of the EU DEMO fusion reactor is currently in the pre-conceptual design phase within the Magnets Work Package (WPMAG) [1], [2]. Three options have been considered up to now for the Toroidal Field coils, based on low-temperature SC cable-in-conduit conductor (CICC) cooled by supercritical He. In the ENEA option [3], two out of six cable petals of this CICC are obtained twisting the strands around a low-impedance spiral-walled channel ("hole"), see Fig. 1, similarly to what is proposed for some of the Korean DEMO conductors [4].

This work was supported by the Euratom research and training programme 2014-2018 under grant agreement No 633053. The views and opinions expressed herein do not necessarily reflect those of the European Commission. *(Corresponding author: R. Bonifetto.)*

R. Bonifetto, L. Savoldi, R. Zanino, and A. Zappatore are with the NEMO Group, Dipartimento Energia, Politecnico di Torino, 10129 Torino, Italy (e-mail: roberto.bonifetto@polito.it, laura.savoldi@polito.it, roberto.zanino@polito.it, andrea.zappatore@polito.it).

P. Bruzzone and B. Stepanov are with SPC EPFL, Villigen 5232, Switzerland (e-mail: pierluigi.bruzzone@psi.ch, boris.stepanov@psi.ch).

V. Corato and L. Muzzi are with ENEA, 00044 Frascati, Italy and also with Italian Consortium for Applied Superconductivity (ICAS), 00044 Frascati, Italy (e-mail: valentina.corato@enea.it, luigi.muzzi@enea.it).

Color versions of one or more of the figures in this paper are available online at http://ieeexplore.ieee.org.

Digital Object Identifier will be inserted here upon acceptance.

As no thermal-hydraulic (TH) characterization was previously available for such a cable prototype, especially in view of its two-hole structure, a full-scale short sample of the wind-and-react1 (WR1) prototype conductor (the same already tested to assess its DC and AC performance [3]), has been tested in 2016 in the right leg of SULTAN at SPC, Villigen (Switzerland). It was equipped with thermometers, pressure taps, a mass flow meter, a differential pressure sensor and two heaters, see Fig. 2a. The main objectives of the tests were:

- the detailed hydraulic characterization of the conductor to allow the assessment / development of the friction factor correlations to be adopted in the numerical analyses of the magnet design [5], [6],
- the TH characterization of the sample, with special reference to the identification of possible uneven temperature distributions on the cross section due to the asymmetric cooling provided by the two holes.

In the paper, the experimental results of the hydraulic and thermal-hydraulic (heat slug) tests are presented first.

Due to the lack of experimental data on the small spiral-

(a) (b)

Fig. 1. Pictures of the CICC sample tested in SULTAN in 2016: (a) cross section and (b) whole sample length. In (b) the red markers following the two holes twisted path are also visible (see the text).

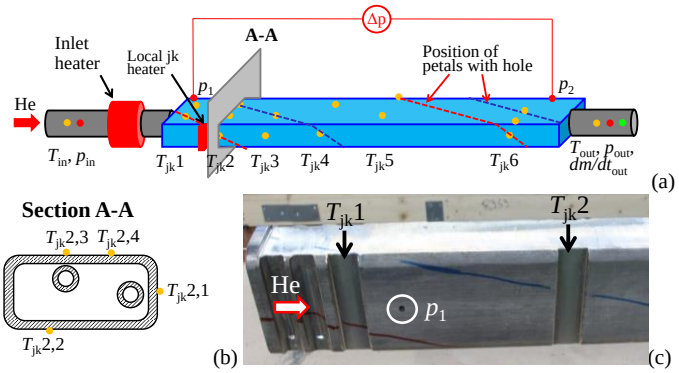

Fig. 2. Sketch of (a) the short sample instrumentation and (b) the azimuthal location of the 4 jacket temperature sensors on section A-A. (c) Picture of the conductor sample after jacket machining (vertical grooves) to fit the temperature sensors; the two markers (red and blue lines) following the projection on the conductor surface of the twisted paths of the two holes are also evident, as well as the small hole in the jacket where the p_1 tap is installed.

walled pipe used for the two holes, a Computational Fluid Dynamics (CFD) analysis is performed to derive a suitable friction factor correlation for that type of spiral. The correlation can be adopted in 1D TH codes (like e.g. the 4C code [7]) for the simulation of this kind of CICC together with existing, validated friction factor correlations for the strands bundle region [8], [9]. The pressure drop obtained applying this set of correlations is then compared with the experimental hydraulic characterization to assess the suitability of the former in order to use it in the simulations for the pre-conceptual design analysis [10], [11].

The heat slug tests performed in SULTAN are also used to calibrate (and validate) a free parameter typically present in the models of the bundle-to-hole heat transfer, by comparing the computed temperature evolution at the different axial locations with the experimental data. An accurate assessment of this parameter is needed to accurately capture the propagation of thermal disturbances along the conductor such as, e.g., the propagation of a quench.

II. Experimental Setup

A. Instrumentation

The sample tested in SULTAN, the main characteristics of which are listed in Table I, was well instrumented from the thermal-hydraulic point of view. The diagnostics included:

- Inlet and outlet temperature (T) and pressure (p) sensors, and outlet mass flow (dm/dt) meter (see also Fig. 3a for their exact location).
- Differential pressure sensor across 2 m of conductor length (Fig. 2a).
- Local jacket temperature (T_{jk}) sensors.

The T_{jk} sensors are quite peculiar of this experiment - before installing them, the poloidal position of the two petals with the hole has been carefully marked on the whole sample length, following their twisted paths, as reported in Fig. 1b and Fig. 2c. At the 6 selected axial locations reported in Fig. 3b, the jacket has been locally machined in order to reduce its thickness to only 2.7 mm, as shown in Fig. 2c. At each location, 4 temperature sensors have been installed at different azimuthal positions on the jacket surface, namely in correspondence of the petals with the two holes and at two intermediate positions, see the sketch in Fig. 2b, aimed at assessing the temperature gradients that could arise on the conductor cross section following the local perturbation induced by the jacket heater.

TABLE I
ENEA TF Conductor Sample Parameters [3]

Parameter	Value
Sample length	2.546 m
Jacket outer dimensions	72[&] mm × 38.8 mm
Jacket inner dimensions	66.6 mm × 25 mm
SC strands (number/diameter)	1080 / 1 mm
Cu strands (number/diameter)	132 / 1.5 mm
Cu / non Cu ratio in SC strands	1
Last cable stage twist pitch	690 mm
Cos(θ)	0.95
Bundle void fraction[$]	24.6%
Wrap area	22 mm^2
He flow area in the bundle	378.6 mm^2
Bundle hydraulic diameter	0.336 mm
Spiral diameter (inner/outer)	4.6 mm / 6.6 mm
Spiral pitch	6.4 mm
Spiral strip width	3.6 mm
Spiral thickness	1 mm

[&] This value is smaller than the nominal one reported in [3] because the jacket has been machined in order to fit in SULTAN.
[$] Measured by image analysis.

B. Heaters

In order to induce thermal perturbations, two heaters were installed on the sample:

- A resistive heater on the inlet pipe, shown in Fig. 4a, used to characterize the CICC hydraulic performance at different operating inlet temperatures T_{in}.
- A jacket heater, shown in Fig. 4b, right upstream of $T_{jk}2$ sensor, aimed at heating only a single petal, namely one of the two petals containing a hole.

III. Test Results

The thermal-hydraulic tests performed include:

- Measurement of the steady state pressure drop for dif-

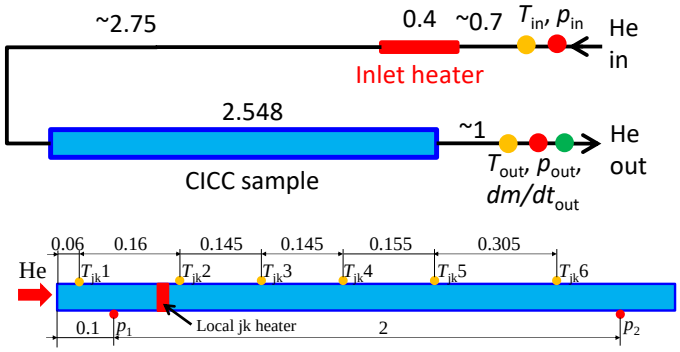

Fig. 3. Sketch of the location of (a) inlet heater, p, T and dm/dt facility sensors, and (b) sensors installed on the sample (all quotes are in m). The inlet and outlet pipes diameter is 6 mm (inner) × 8 mm (outer).

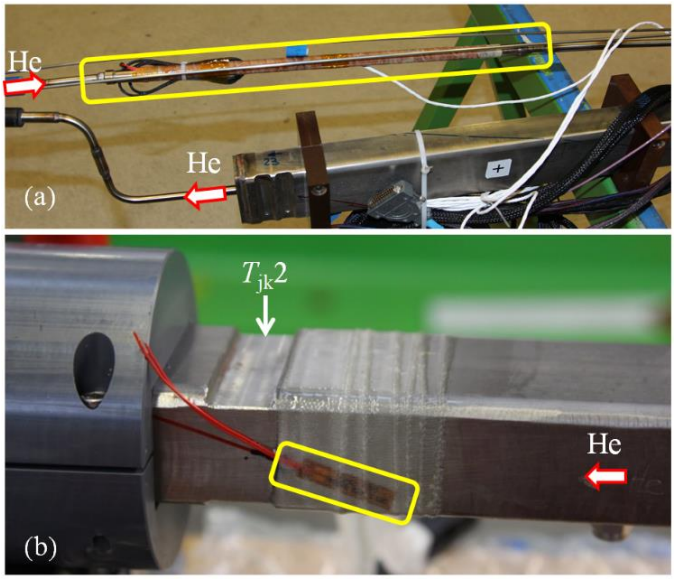

Fig. 4. Picture of (a) the resistive heater installed on the inlet pipe and (b) the local jacket heater installed few centimeters upstream the $T_{jk}2$ set of thermometers.

ferent mass flow rates at different T_{in}, aiming at the hydraulic characterization of the conductor

- Propagation of heat slug tests induced by the heater on the inlet pipe, at different mass flow rates and input power, aiming at the measurement of the average He speed in the conduit
- Propagation of heat slug tests induced by the local heater on the conductor jacket, at different mass flow rates and input power, aiming at the assessment of the temperature homogenization on the conductor cross section.

A summary of the hydraulic and TH tests is reported in Table II and Table III, respectively.

A. *Hydraulic tests*

During the hydraulic tests, the mass flow rate was reduced stepwise from the maximum to the minimum values acting on a control valve, while keeping the inlet pressure constant at ~10 bar. The T_{in} was then also changed by a manual control of the inlet heater input power. These conditions were kept constant for a sufficiently long time, in order to measure the hydraulic performance only when steady state flow conditions were reached in the whole sample. The evolution of the mass flow rate and pressure drop along the conductor for a typical shot (constant T_{in}) are reported in Fig. 5.

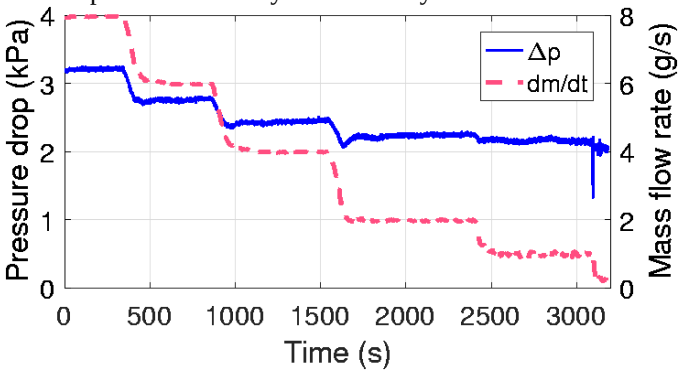

Fig. 5. Evolution of measured pressure drop (solid, left axis) and mass flow rate (dashed, right axis) for shot ENEAa180702 (T_{in} ~6 K).

TABLE II
SUMMARY OF HYDRAULIC TESTS

Shot	T_{in} (K)	*dm/dt* (g/s)
ENEAa180701	4.5	~0, 2, 4, 6, 8, 10
ENEAa180702	6	~0, 1, 2, 4, 6, 8
ENEAa180703	8.5	~0, 1, 2, 3
ENEAa180704	11	~0, 1, 1.5, 2
ENEAa180705	13.5	~0, 1, 1.5

TABLE III
SUMMARY OF THERMAL-HYDRAULIC TESTS (T_{IN} = 4.5 K)

Shot	*dm/dt* (g/s)	Inlet heater (W)	Jk heater (W)
ENEAb190702	7	20	0
ENEAb190703		40	0
ENEAb190704		0	10
ENEAb190705		0	15
ENEAb190706	5	20	0
ENEAb190707		40	0
ENEAb190708		0	10
ENEAb190709		0	15
ENEAb190710	3	20	0
ENEAb190711		40	0
ENEAb190712		0	10
ENEAb190713		0	15

Fig. 6 shows the measured hydraulic characteristic of the CICC sample at different temperature values. The experimental points correspond to the average value of pressure drop and mass flow rate during at least ~100 s steady state operating conditions (the plateau in Fig. 5). The offset in the pressure drop measurement (value at ~0 g/s) has been removed. The error bar is due to nominal Δp and *dm/dt* sensors accuracy (±60 Pa and ±20 mg/s, respectively) summed to the uncertainty due to the measured signal oscillations (~±25 Pa and ~±10 mg/s, respectively). The progressive increase of the pressure drop at constant mass flow rate for increasing He

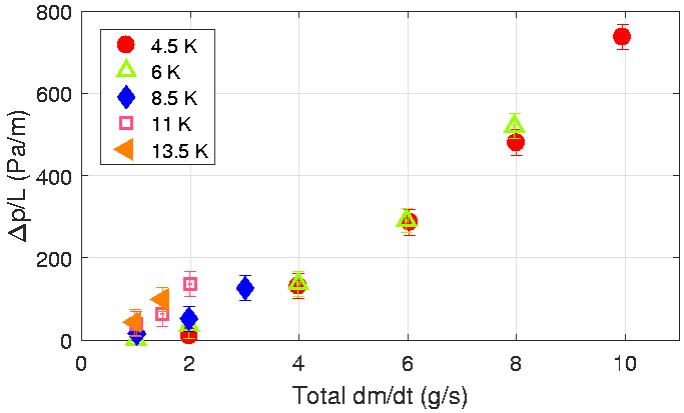

Fig. 6. Steady state experimental data collected during the sample hydraulic characterization, for different inlet temperature values. The error bars are due to sensors accuracy and to the uncertainty introduced by the measured signal oscillations. The mass flow rate on the *x*-axis is the total (bundle region + holes) mass flow rate in the CICC.

temperature is due to the fact that (at the first order approximation) $\Delta p \propto 1/\rho$, where ρ is the He density, for constant dm/dt, and the density reduces of a factor ≥3 from 4.5 K to 13.5 K.

B. *Thermal-hydraulic tests*

The propagation of a heat slug driven by the inlet resistive heater is shown in Fig. 7. The jacket thermometers at the same axial location (represented with the same color in Fig. 7) but at different azimuthal position are pretty consistent with each other, with some small (on average within 0.1 K, after removing the initial offset) difference. The heat slug advection from the inlet (T_{jk}1.x sensors) to the sample mid-length (T_{jk}6.x sensors) and to the outlet thermometer (T_{out}) is evident from the location of the different temperature peaks. The temperature evolution at the T_{jk}1.x sensors in fact resembles the square-waveform of the power deposition (40 W for 5 s, in this specific shot), while during the propagation along the sample the heat and mass transfer between holes and the bundle causes the broadening and lowering of the thermal disturbance. Note that due to a short circuit with the jacket, data from sensor T_{jk}5.2 have been discarded.

The propagation of a heat slug driven by the local jacket heater is reported in Fig. 8. The T_{jk} sensors highlight that the heating is localized just upstream the T_{jk}2 sensors, and precisely on the jacket surface in correspondence of the petal with the hottest among all T_{jk}2.x sensors, see Fig. 8a. The maximum temperature among T_{jk}3.x sensors is measured by T_{jk}3.3 sensor, i.e. the one measuring the T_{jk} in correspondence of the petal containing the other hole. The characteristic time of heat diffusion among the T_{jk}2.x and T_{jk}3.x sensors along the steel jacket is ~1000 s, i.e. >> ~1 s (the He advection time along the same distance); this means that the (warm) He path is not that much constrained inside the twisted hole, but it can travel (and advect heat) along paths almost parallel to the conduit axis, crossing the spiral gaps and exchanging heat in an efficient way with the neighboring petals. The quasi-3D representation of the petal temperature distribution measured along the conduit reported in Fig. 9 confirms that the hot spot on the conductor cross section remains at the azimuthal location of the heater also in correspondence of T_{jk}3 section. This means that

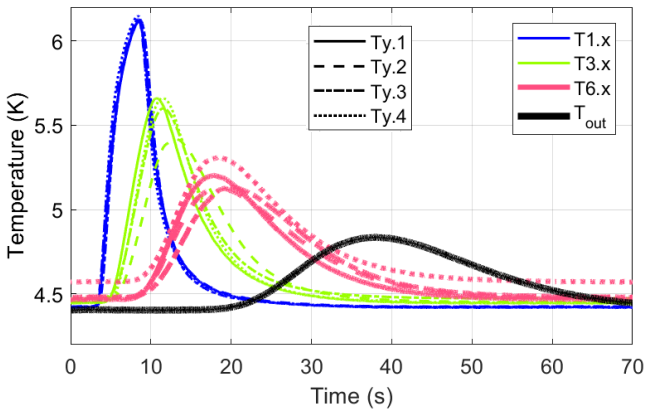

Fig. 7. Evolution of the measured temperature during heat slug test ENEAb190707. The uncertainty on the measured temperature (±2 mK) is not reported because cannot be appreciated on this scale.

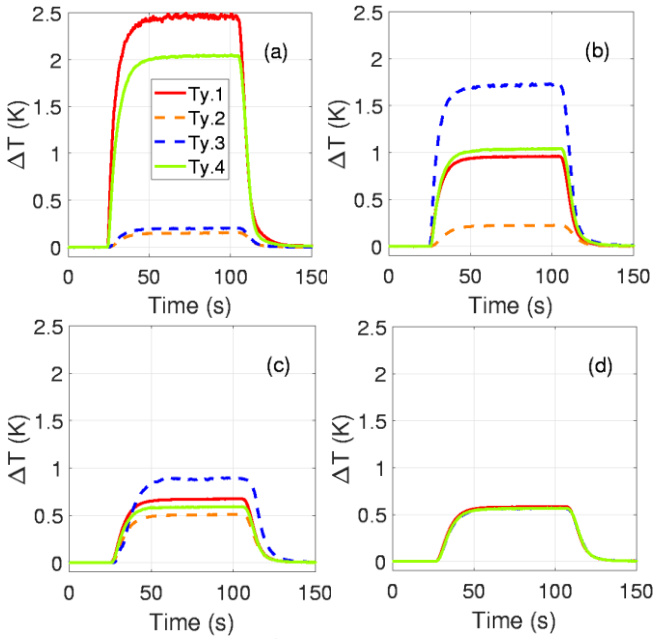

Fig. 8. Measured evolution of the jacket temperature at T_{jk}2 (a), T_{jk}3 (b), T_{jk}4 (c) and T_{jk}5 (d) during a heat slug propagation test (shot ENEAb190705), performed energizing only the local jacket heater just upstream T_{jk}2.

either the heat conduction along the conductor dominates the heat conduction across the conductor cross section, or (more likely, as mentioned above) the He flow is mostly axial and poorly affected by the petal twist, so that the heat is advected mainly axially. Moreover, from Fig. 9 it is evident that a local thermal perturbation will be redistributed across the conductor cross section, leading to a homogeneous temperature distribution, well within one twist pitch of the last cabling stage. At T_{jk}5 section the temperature is indeed already uniform on the conductor cross section, at a distance ~0.45 m (see Fig. 3b) < ¾·0.69 m (twist pitch of the last cabling stage, see Table I).

This implies that, notwithstanding the (apparently) asymmetric cooling provided by two separate holes, available 1D

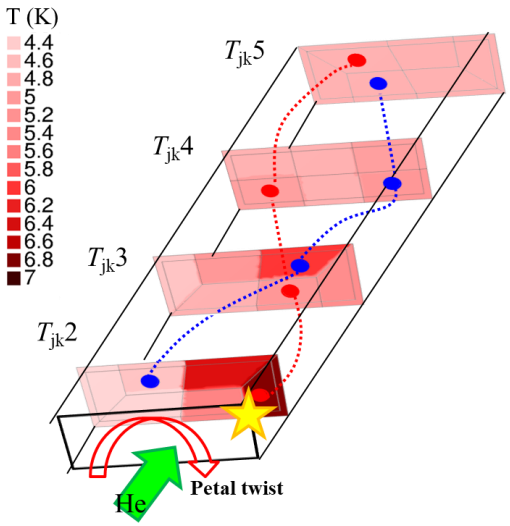

Fig. 9. Steady state temperature distribution measured on the different cross sections of the CICC sample during shot ENEAb190705, performed energizing only the local jacket heater (yellow star) just upstream T_{jk}2. The holes twisted paths are also reported.

numerical tools are still applicable to analyze the behavior of the CICC proposed by ENEA; this is true provided that the distance from the (local) thermal perturbation is > ~half of the last cabling stage twist pitch, for CICCs with aspect ratio and jacket dimensions comparable with those of the sample at hand.

IV. CFD ANALYSIS OF THE HOLE

The hydraulic characterization extracted from the experiment results can be used to assess the friction factor correlations to be adopted in the TH simulations in the magnets design phase. However, while for the bundle region such correlation is already available [8], [9], for a low-impedance channel with a flat-spiral having an inner diameter of 5 mm no correlations are available. Due to the lack of measured pressure drop data on such a small spiral, it is not possible to obtain a correlation starting from experimental data as done in the past [12]. For this reason, in this Section a CFD model is generated and used to perform numerical simulations. The computed operating points are used to deduce the friction factor correlation for the hole, following the approach adopted in [13], [14].

A. CFD model

The CFD analysis of the spiral of one DEMO TF conductor has been performed using the commercial software STAR-CCM+ v11.04.012 [15].

The computational domain adopted for the analysis is a ~23-pitch-long portion of the hole, much longer than the single-pitch domain usually analyzed [14], to capture the periodic flow pattern induced by the spiral wall.

The spiral is assumed to be straight, even though it is twisted together with the last cabling stage. This assumption is justified by the fact that the pitch of the spiral is much smaller that the twist pitch of the last cabling stage, therefore the influence of the spiral twist in the cable on the flow field is neglected here. No mass transfer is supposed to take place between the hole and the bundle (the latter is not modeled).

The simulations have been performed using the following models:

- Pure hydraulic, 3D, steady state, incompressible flow.
- k-ω Shear Stress Transport (SST-Menter) turbulence model [16] with all y+ wall treatment
- Constant properties (density ρ and dynamic viscosity μ)

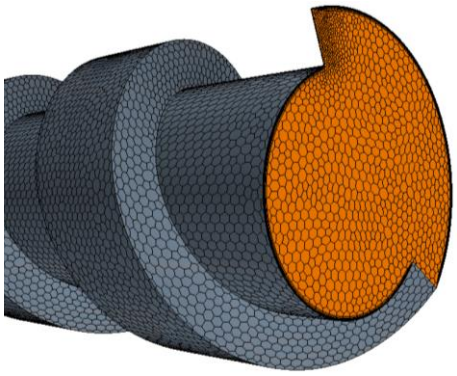

Fig. 10. Zoom of the meshed geometry (outlet region).

Note that the He properties were adjusted depending on the corresponding experimental He inlet temperature (and pressure, i.e. ~10 bar) considered.

Concerning the mesh generation, a careful mesh independence study has been performed. The resulting mesh, shown in Fig. 10, is composed by 1.3 million cells, including polyhedra and eight prism layers for the near-wall treatment.

B. Simulation setup

The boundary conditions adopted for all the simulations are the following:

- Inlet: imposed mass flow rate and temperature (a uniform velocity profile is assumed at the inlet cross section)
- Outlet: zero pressure (gauge)

The inlet temperature range considered in the CFD analysis is the same of the experiment. On the other hand, we avoid to simulate all the mass flow rate values tested in the experiment if they were very close. However, we introduced, especially at high temperature (11 K and 13.5 K), additional mass flow rate values, in order to have more points and to define better the region at higher *Re*, which is also the DEMO operating condition, see below.

C. Results

The velocity field resulting from the CFD analysis is pre-

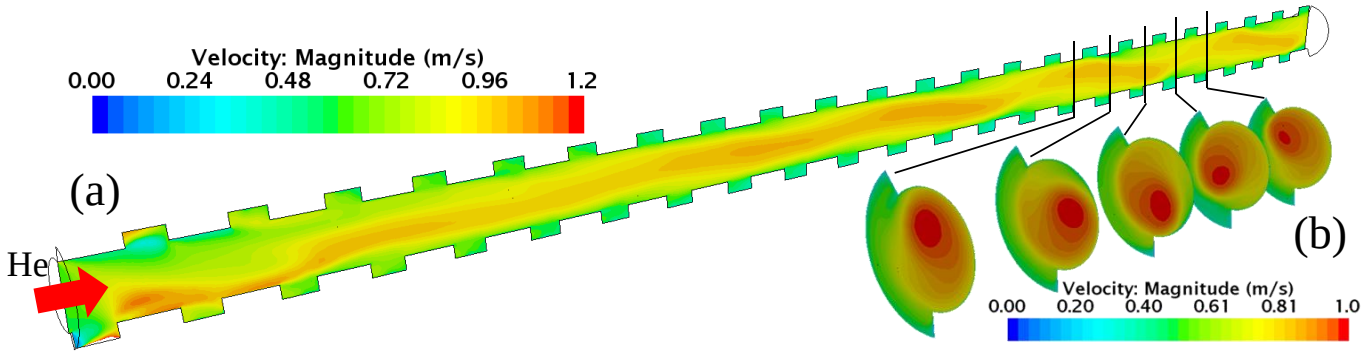

Fig. 11. (a) Velocity field on a longitudinal cross section of a hole. The inlet is located on the left. (b) Velocity field on five cross sections, distant one pitch from each other.

sented in Fig. 11. After the entry effect that lasts for ~10 pitches, a periodic flow field is achieved. Furthermore, the period is ~5 pitches long and this justifies the choice not to have a single pitch with periodic boundary conditions.

The periodic flow under discussion can be observed in Fig. 11b. The azimuthal location where the maximum velocity is computed on successive pitch cross sections is moving in clockwise direction (looking in the flow direction) as the fluid moves along the spiral. This secondary flow is driven by the pitch of the spiral itself, and this macroscopic motion has to be taken into account since it influences the pressure drop computation.

The Blasius friction factor (f_{Bl}) has been obtained from the simulation using (1):

$$f_{Bl} = 2\frac{D}{L}\frac{\Delta p}{\rho v^2} \tag{1}$$

where D is the hole internal diameter, the pressure drop Δp has been computed across a length L equal to a 10-pitch-long period close to the outlet and the velocity (v) has been computed as the mass flow average over the two cross sections used to evaluate the Δp, see Fig. 11b.

The f_{Bl} values obtained from the simulations are reported as a function of the Reynolds number $Re = \rho v D/\mu$ in Fig. 12, and they are well fitted ($R^2 = 0.95$) by the power law in (2)

$$f_{Bl}(\mathrm{Re}) = 0.1687 \cdot \mathrm{Re}^{-0.1129} \tag{2}$$

V. Thermal-Hydraulic Characterization

A. Hydraulic characterization

The correlation developed by the CFD simulations in previous Section, valid for this specific spiral in the operating range tested in this experimental campaign (fully representative of the real DEMO TF coils one), is used here for the calculation of the friction factor in the two holes of the ENEA DEMO TF conductor proposal. Note that the holes have been considered circular for their entire length (as no total nor even partial collapse of the spiral during the conductor squeezing has been considered) since a CICC piece autopsy has shown a small (plastic) ellipticity (~1.3) [3].

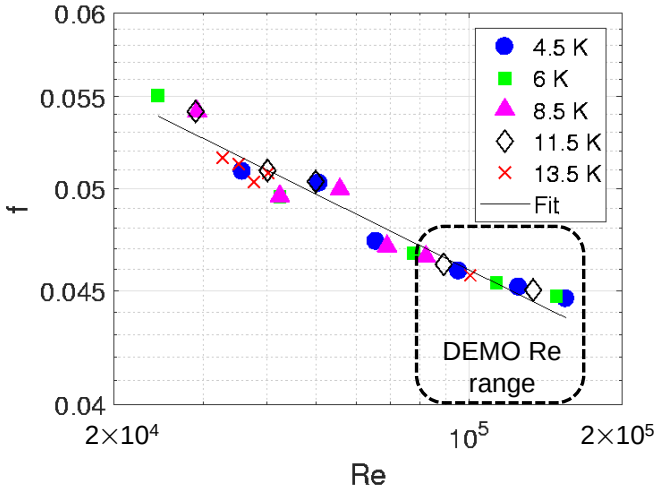

Fig. 12. Hole friction factor computed by the CFD simulations vs. *Re* for different inlet temperature values (symbols). The power-law best fit (2) is also shown, together with the foreseen DEMO operational range.

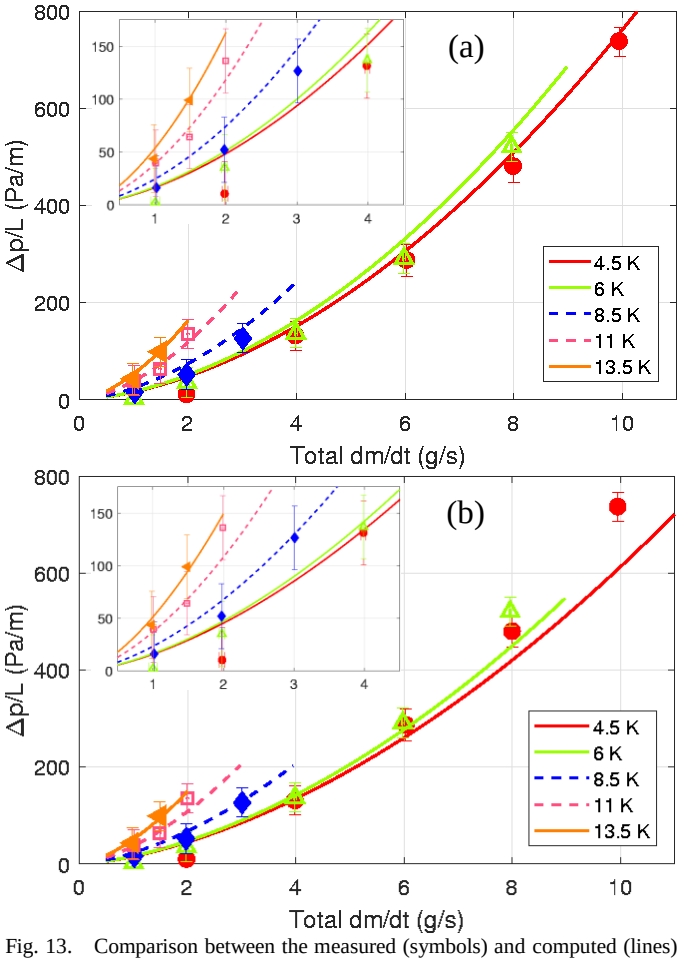

Fig. 13. Comparison between the measured (symbols) and computed (lines) hydraulic characteristic of the sample on the whole range tested in the experimental campaign, for different inlet temperature values, using for the bundle region either the correlation from [8] (a) or from [9] (b); a zoom at low mass flow rates is reported in the inset. The error bars are due to sensors accuracy and to the values oscillation during data acquisition. The mass flow rate on the *x*-axis is the total mass flow rate in the CICC.

For a bundle region featuring a so low void fraction, two correlations based on the Darcy-Forchheimer momentum balance equation for the flow in porous media are available, namely those proposed in [8] and [9]. Both of them should however be considered with a caveat: the permeability depends on the porosity only and not, as it should, also on the tortuosity and so on the different cabling twist pitches. They were developed for a wide range of bundle void fractions (between 25% and 45%) and based on an experimental database where $10 < Re < 14000$ (for the sample during the tests, as well as in DEMO-relevant operating conditions, $60 < Re < 1000$ in the bundle). The resulting two characterizations are compared with the experimental data collected on the CICC sample tested in SULTAN, and the results of the comparisons are reported in Fig. 13 in the dimensioned (Δp vs. dm/dt) plane. For all the different inlet temperatures (from the nominal value of 4.5 K up to 13.5 K) the agreement between the measurement and the characteristic predicted by the set of

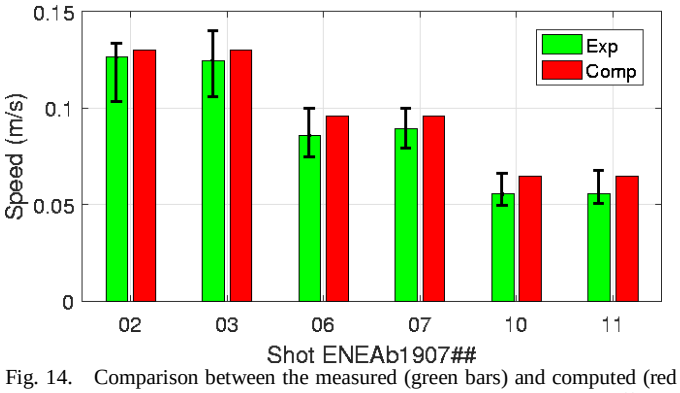

Fig. 14. Comparison between the measured (green bars) and computed (red bars) He average speed in the sample. The error bars are due to the different times at which the 4 temperature sensors at $T_{jk}1$ and $T_{jk}6$ reach the peak value.

correlations adopting the bundle friction factor recipe described in [8] is within the experimental error bar, see Fig. 13a. On the other hand, the pressure drop at higher mass flow rates is underestimated by the set of correlations adopting the bundle friction factor recipe described in [9], as reported in Fig. 13b. For this reason, and according to [17], the bundle friction factor correlation developed in [8] is used from now on.

It is well known that the temperature wave in the conduit travels with the average He speed in the cross section [18]. The He speed can be estimated experimentally evaluating the He transit time Δt between the $T_{jk}1$ and $T_{jk}6$ sets of sensors (estimated as the difference between the times at which the average temperature signal reaches its peak), and knowing the distance between the two (Δx). The average speed v_{ave} is then estimated as $\Delta x/\Delta t$, as far as the experiment is concerned, while it can be evaluated as area-weighted average of the computed bundle and hole speed in the simulations. The latter have been performed with a 4C model of the sample including the sample itself and the circuit of the facility up to the *p*, *T* and *dm/dt* sensors reported in Fig. 3. The simulations have been performed starting from an initial *T*, *p* and *dm/dt* equal to the experimental ones. Then the experimental p_{in} and p_{out} have been prescribed as boundary conditions at the respective sensors locations. Fig. 14 reports the comparison between the average He speed in the conduit estimated from experimental data (see e.g. Fig. 7) and the computed one. While for a prescribed mass flow rate there are infinite combinations of bundle and hole friction factor correlations fitting the experimental v_{ave}, only one among these sets is also fitting the experimental pressure drop. The set adopted in the 4C model is the same proven to capture the pressure drop, as documented in Fig. 13a. As the experimental pressure drop (and not the mass flow rate) is prescribed in the simulation, the good agreement (always within the experimental error bar) on the average He speed shown in Fig. 14 confirms that also the mass flow rate repartition between holes and bundle in the CICC is properly captured: it is computed to be in the proportion 55%-45%, respectively. This also confirms the adequacy of the assumption of circular holes everywhere.

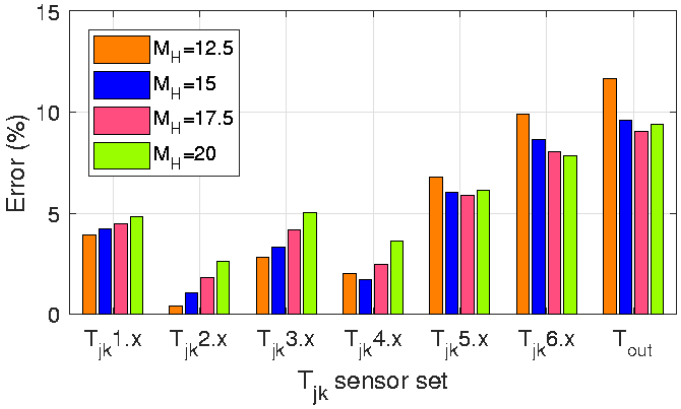

Fig. 15. Error between the computed and measured temperature evolutions at the instrumented sections of the sample during heat slug shot ENEAb190707, used for the bundle-to-hole heat transfer multiplier (M_H) calibration.

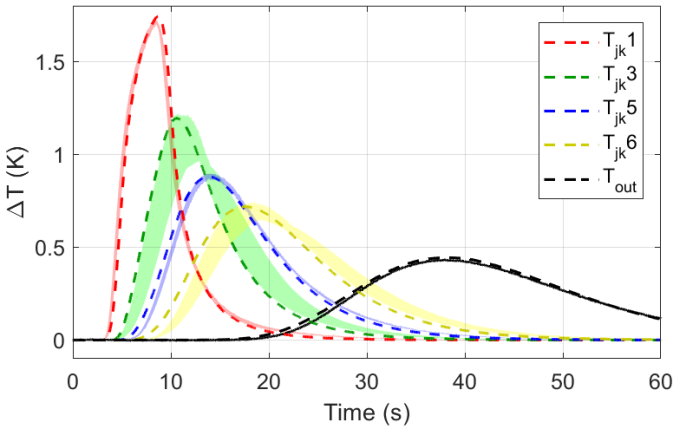

Fig. 16. Comparison between the computed and measured temperature evolutions at the instrumented sections of the sample during heat slug shot ENEAb190707, used for the bundle-to-hole heat transfer multiplier (M_H) calibration. The colored areas are the envelope of the T_{jk}y.x measured by T_{jk}y sets of sensors.

B. *Thermal-hydraulic characterization*

In view of the tight thermal coupling between the holes and the bundle, demonstrated in the experiment by the fast temperature homogenization across the conductor cross section, an accurate calibration of this heat transfer mechanism is needed by the numerical tools used for the design of the DEMO TF magnets, especially to perform reliable quench simulations [19]. Here the heat slug tests performed energizing the inlet heater are used to calibrate the above-mentioned thermal coupling in the 4C TH code [7].

In the 4C model of a DEMO TF coil, described in detail in [6], [10] and [11], the heat transfer between the two regions (holes and bundle) is computed as the parallel of two thermal resistances across the spiral, similarly to what is done in [20] and as suggested in [17], and namely:

- the series of hole-spiral boundary layer + spiral wall + spiral-bundle boundary layer (weighted with the unperforated fraction of spiral)
- the series of hole-wall boundary layer + wall-bundle boundary layer, that qualitatively accounts for the heat transfer across the spiral gap.

The heat transfer due to mass exchange is also separately accounted for.

The boundary layer heat transfer coefficient is derived from the Nusselt number, computed (for turbulent flow) using the Dittus-Boelter correlation [21], as suggested in [17]. The heat transfer across the spiral gap is the most uncertain one, and in the model a suitable multiplier $M_H > 1$ is included, to account for the effects of local turbulence. The calibration of M_H has been performed minimizing the average error in the computed temperature evolution at each T_{jk} location (including also the outlet T sensor) with respect to the measured evolution. Being the latter measured at several azimuthal locations, the error has been computed as distance from the envelope of minimum and maximum temperature values measured at the same axial location.

The same 4C model of the sample adopted in previous Section is used here, energizing the inlet heater (also included in the model) according to the experimental power value. The results for the scanned M_H range (from 12.5 to 20) are reported in Fig. 15. The typical value of M_H for ITER-like conductors, featuring straight low-impedance channels with a minimum inner diameter of 7 mm (Japanese Central Solenoid conductor CSJA [22]), is ~10 (see e.g. [19]). In the present case, the M_H value for which the average value of the error on all sensors is minimized is 17.5. This larger value if compared with ITER-like conductors can be justified by a higher He turbulence in the spiral gaps, due to the increased thickness-to-diameter ratio for such a small spiral (inner diameter 5 mm, see Table I, being the 1 mm thickness unchanged). The enhanced bundle-to-hole heat transfer confirms and justifies the fast temperature homogenization on the conductor cross section following a localized thermal disturbance, see Fig. 9. The error between the computed and measured temperature evolutions (see Fig. 15) increases for increasing distance from the inlet because it is normalized with respect to the maximum temperature increase in correspondence of the specific T_{jk}y section, which decreases for increasing distance from the inlet. Therefore, an absolute error (peak ~50-80 mK, average ~20 mK) comparable for all T_{jk}y sensors results in the increasing relative error reported in Fig. 15.

The comparison between the computed and measured temperature evolutions with the optimum M_H multiplier is reported in Fig. 16, showing an excellent agreement (average error within 5%). In order to confirm the calibration, it was validated on another heat slug shot, not used for the calibration, see Fig. 17, showing again a very good agreement.

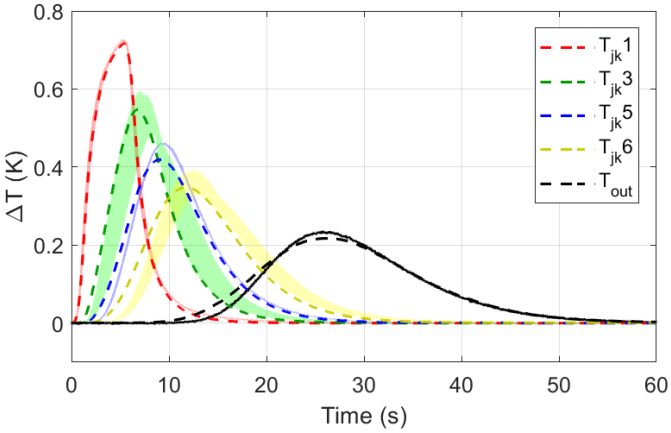

Fig. 17. Comparison between the computed and measured temperature evolutions at the instrumented sections of the sample during heat slug shot ENEAb190702. The colored areas are the envelope of the T_{jk}y.x measured by T_{jk}y sets of sensors.

VI. Conclusions and Perspective

Dedicated thermal-hydraulic tests were performed in SULTAN in 2016 on a full-size, short length sample conductor, proposed by ENEA for the EU DEMO Toroidal Field coils. The detailed instrumentation allowed to retrieve its hydraulic characteristic and to assess that the response to a (azimuthally and axially) localized heating becomes roughly uniform on the conductor cross section at a distance of ~3/4 of the final cabling stage twist pitch from the heater, for the ENEA sample at hand.

A set of Computational Fluid Dynamics (CFD) simulations has then been carried out in order to compute a friction factor for the hole (5 mm inner diameter). This friction factor correlation, together with the correlation based on the Darcy-Forchheimer momentum balance equation for the friction in the bundle region, was shown to accurately reproduce the measured hydraulic characteristic of the conductor.

The hole-to-bundle thermal coupling has also been calibrated in the 4C thermal-hydraulic code, exploiting the heat slugs performed in the sample.

In perspective, the newly developed friction factor correlation for the hole and the calibrated hole-to-bundle heat transfer multiplier will be adopted in the analysis of the ENEA proposal for the EU DEMO TF winding pack, including cyclic plasma burn and quench analyses.

Acknowledgement

This work has been carried out within the framework of the EUROfusion Consortium. The views and opinions expressed herein do not necessarily reflect those of the European Commission.

References

[1] L. Zani, C. M. Bayer, M. E. Biancolini, R. Bonifetto, P. Bruzzone, C. Brutti, D. Ciazynski, M. Coleman, I. Duran, M. Eisterer, W.H. Fietz, P.V. Gade, E. Gaio, F. Giorgetti, W. Goldacker, F. Gömöry, X. Granados, R. Heller, P. Hertout, C. Hoa, A. Kario, B. Lacroix, M. Lewandowska, A. Maistrello, L. Muzzi, A. Nijhuis, F. Nunio, A. Panin, T. Petrisor, J-M. Poncet, R. Prokopec, M. Sanmarti Cardona, L. Savoldi, S.I. Schlachter, K. Sedlak, B. Stepanov, I. Tiseanu, A. Torre, S. Turtù, R. Vallcorba, M. Vojenciak, K.-P. Weiss, R. Wesche, K. Yagotintsev, and R. Zanino, "Overview of Progress on the EU DEMO Reactor Magnet System Design", *IEEE Trans. Appl. Supercond.*, vol. 26, no. 4, Jun. 2016, Art. no. 4204505.

[2] V. Corato, M. E. Biancolini, R. Bonifetto, P. Bruzzone, D. Ciazynski, M. Coleman, A. della Corte, A. Dembkowska, M. Eisterer, W.H. Fietz, E. Gaio, F. Giorgetti, R. Heller, B. Lacroix, M. Lewandowska, A. Maistrello, L. Muzzi, A. Nijhuis, F. Nunio, A. Panin, L. Savoldi, K. Sedlak, B. Stepanov, G. Tomassetti, A. Torre, S. Turtù, D. Uglietti, A. Vaccaro, R. Vallcorba, K.-P. Weiss, R. Wesche, M. Wolf, L. Zani, and R. Zanino, "EU Progress in Superconductor Technology Development

for DEMO Magnets," presented at ISFNT (2017), and submitted to *Fus. Eng. Des*.

[3] L. Muzzi, L. Affinito, S. Chiarelli, V. Corato, A. della Corte, A. Di Zenobio, R. Freda, S. Turtù, A. Anemona, R. Righetti, A. Bragagni, M. Seri, F. Gabiccini, G. Roveta, A. Aveta, S. Galignano, P. Bruzzone, K. Sedlak, B. Stepanov, and R. Wesche, "Design, Manufacture, and Test of an 80 kA-Class Nb_3Sn Cable-In-Conduit Conductor With Rectangular Geometry and Distributed Pressure Relief Channels," *IEEE Trans. Appl. Supercond.*, vol. 27, no. 4, Jun. 2017, Art. no. 4800206.

[4] K. Kim, S. Oh, J. S. Park, C. Lee, K. Im, H. C. Kim, G.-S. Lee, G. Neilson, T. Brown, C. Kessel, P. Titus, and Y. Zhai, "Conceptual design study of the K-DEMO magnet system", *Fus. Eng. Des.*, vol. 96-97, 2015, pp. 281-285.

[5] M. Lewandowska, K. Sedlak, and L. Zani, "Thermal-Hydraulic Analysis of the Low-T_c Superconductor (LTS) Winding Pack Design Concepts for the DEMO Toroidal Field (TF) Coil," *IEEE Trans. Appl. Supercond.*, vol. 26, no. 4, Jun. 2016, Art. no. 4205305.

[6] R. Zanino, R. Bonifetto, O. Dicuonzo, L. Muzzi, G. F. Nallo, L. Savoldi, and S. Turtù, "Development of a Thermal-Hydraulic Model for the European DEMO TF Coil," *IEEE Trans. Appl. Supercond.*, vol. 26, no. 3, Apr. 2016, Art. no. 4201606.

[7] L. Savoldi Richard, F. Casella, B. Fiori, and R. Zanino, "The 4C code for the cryogenic circuit conductor and coil modeling in ITER," *Cryogenics*, vol. 50, no. 3, Mar. 2010, pp. 167-176.

[8] M. Bagnasco, L. Bottura, and M. Lewandowska, "Friction factor correlation for CICC's based on a porous media analogy," *Cryogenics*, vol. 50, 2010, pp. 711-719.

[9] M. Lewandowska, and M. Bagnasco, "Modified friction factor correlation for CICC's based on a porous media analogy," *Cryogenics*, vol. 51, 2011, pp. 541-545.

[10] L. Savoldi, R. Bonifetto, A. Brighenti, V. Corato, L. Muzzi, S. Turtù, and R. Zanino, "Performance analysis of a graded winding pack design for the EU DEMO TF coil in normal and off-normal conditions," *Fus. Eng. Des.*, vol. 124, Nov. 2017, pp. 45-48.

[11] L. Savoldi, R. Bonifetto, A. Brighenti, V. Corato, L. Muzzi, S. Turtu', R. Zanino, and A. Zappatore, "Quench propagation in a TF coil of the EU DEMO," *Fus. Sci. Technol.*, vol. 72, no. 3, Oct. 2017, pp. 439-448.

[12] R. Zanino, P. Santagati, L. Savoldi Richard, A. Martinez, and S. Nicollet, "Friction factor correlation with application to the central cooling channel of cable-in-conduit super-conductors for fusion magnets," *IEEE Trans. Appl. Supercond.*, vol. 10, 2000, pp. 1066-1069.

[13] R. Zanino, S. Giors and L. Savoldi Richard, "CFD modeling of ITER cable-in-conduit superconductors. Part III: correlation for the central channel friction factor," *proceedings of the 21th International Cryogenic Engineering Conference (ICEC21)*, vol. 1, 2007, pp. 207-211.

[14] R. Zanino, S. Giors, and R. Mondino, "CFD Modeling of ITER Cable-in-Conduit Superconductors. Part I: Friction in the Central Channel," *Adv. Cryo. Eng.*, vol. 823, no. 1, May 2006, pp. 1009-1016.

[15] Star-CCM+ User's Manual 11.04, CD ADAPCO, New York, 2016.

[16] F. R. Menter, "Review of the shear-stress transport turbulence model experience from an industrial perspective," *Int. J. Comput. Fluid Dyn*., vol. 23, no. 4, 2009, pp. 305-316.

[17] L. Savoldi, and R. Zanino, "Common approach for thermal-hydraulic calculations," EFDA_D_2LMECE, v1.2, 16/09/2016.

[18] L. Bottura, "Thermohydraulics of CICC's with Central Cooling Passage," *IEEE Trans. Appl. Supercond.*, vol. 5, no. 2, Jun. 1995, pp. 745-748.

[19] R. Bonifetto, T. Isono, N. Martovetsky, L. Savoldi, and R. Zanino, "Analysis of Quench Propagation in the ITER Central Solenoid Insert (CSI) Coil," *IEEE Trans. Appl. Supercond.*, vol. 27, no. 4, Jun. 2017, Art. no. 4700308.

[20] M. Lewandowska, and L. Malinowski, "Transverse heat transfer coefficient in the dual channel ITER TF CICCs. Part III: Direct method of assessment," *Cryogenics*, vol. 73, 2016, pp. 91-100.

[21] F. Incropera, and D. Dewitt, "Fundamentals of heat and mass transfer," John Wiley & Sons, 2006, 6th edition.

[22] A. Devred, I. Backbier, D. Bessette, G. Bevillard, M. Gardner, C. Jong, F. Lillaz, N. Mitchell, G. Romano, and A. Vostner, "Challenges and status of ITER conductor production," *Supercond. Sci. Technol.*, vol. 27, 2014, Art. no. 044001.